

Aqueous Organic Batteries

Revealing Hydrogen Bond Effect in Rechargeable Aqueous Zinc-Organic Batteries

 Jun Guo⁺, Jia-Yi Du⁺, Wan-Qiang Liu,^{*} Gang Huang,^{*} and Xin-Bo Zhang^{*}

Abstract: The surrounding hydrogen bond (H-bond) interaction around the active sites plays indispensable functions in enabling the organic electrode materials (OEMs) to fulfill their roles as ion reservoirs in aqueous zinc-organic batteries (ZOBs). Despite important, there are still no works could fully shed its real effects light on. Herein, quinone-based small molecules with a H-bond evolution model has been rationally selected to disclose the regulation and equilibration of H-bond interaction between OEMs, and OEM and the electrolyte. It has been found that only a suitable H-bond interaction could make the OEMs fully liberate their potential performance. Accordingly, the 2,5-diaminocyclohexa-2,5-diene-1,4-dione (DABQ) with elaborately designed H-bond structure exhibits a capacity of 193.3 mAhg⁻¹ at a record-high mass loading of 66.2 mgcm⁻² and 100% capacity retention after 1500 cycles at 5 Ag⁻¹. In addition, the DABQ//Zn battery also possesses air-rechargeable ability by utilizing the chemistry redox of proton. Our results put forward a specific pathway to precise utilization of H-bond to liberate the performance of OEMs.

Introduction

Li-ion batteries (LIBs) have been extensively used in portable electronics and electric vehicles over the past decade.^[1,2] However, the limited lithium resources and potential safety risks make them not suitable for large-scale energy storage.^[3] To this end, rechargeable aqueous Zn-ion batteries (ZIBs) have become a favorable candidate due to their intrinsic safe features and the abundant resources, high theoretical specific capacity (820 mAhg⁻¹), and low redox potential (−0.76 V versus SHE) of zinc metal anode.^[4]

Nevertheless, the real-world implementation of ZIBs is still full of thorns due to the lack of suitable cathode materials. Among the available cathode materials, inorganic materials, like MnO₂, V₂O₅, and Prussian blue analogues, etc., follow an intercalation/conversion mechanism during the ion storage/release process. These mechanisms are usually accompanied by large volume and crystal lattice changes, causing the pulverization of inorganic materials and thus leading to rapid capacity decay and unsatisfied cycle life.^[5] Different from inorganic materials, organic electrode materials (OEMs) with soft lattices possess a special coordination mechanism for the ion storage/release, which can readily accommodate the facile storage of Zn²⁺.^[6–8] Moreover, OEMs are primarily composed of naturally abundant elements, such as C, N, and O, enabling them with structural flexibility, environmental friendliness, and resource renewability. Especially, the ubiquitous small quinone-based molecules in living organisms could undergo normal physiological processes with the enolate–carbonyl redox chemistry between quinone and hydroquinone.^[9] This unique redox activity makes them a kind of promising OEMs for ZIBs. Despite promising, like all small organic molecules, these quinone-based OEMs also suffer from the disadvantages of low utilization of active sites, poor electrical conductivity, and easy dissolution in aqueous electrolytes.^[10,11] The generally effective modification methods, such as polymerization or composite with carbon-based materials, cannot fundamentally solve the above problems and usually accompany by the reduction of the theoretical specific capacity of monomers or the energy density of batteries.^[12] To take full advantage of the powerful weak interaction between the molecules through rational structural design would be good choices.

H-bond plays crucial roles in numerous natural and proton transfer processes due to their unique physicochemical properties and the diverse interactions they can engage in.^[13] In aqueous batteries with acid/weak acid electrolytes, there is also existing H-bond that could participate in the entire electrochemical process. However, till now, the real effects of H-bond in aqueous batteries remain poorly understand, and we only have a vague awareness of its role that might stabilize the molecules or facilitate the proton transfer process.^[14–16] Generally, the utilization of active sites and the cycle stability of small molecules are determined by the interactions between molecules, and molecule and the electrolyte. When H-bond forms between the active molecule and electrolyte, the resulted enhanced interaction will bring better electrolyte wettability and reduced coordination difficulty for ions to the molecules, improving the utilization

[*] J. Guo,⁺ Prof. W.-Q. Liu

School of Materials Science and Engineering, Changchun University of Science and Technology, Changchun 130022, China
 E-mail: wqliu1979@126.com

J. Guo,⁺ J.-Y. Du,⁺ Prof. G. Huang, Prof. X.-B. Zhang
 State Key Laboratory of Rare Earth Resource Utilization, Changchun Institute of Applied Chemistry, Chinese Academy of Sciences, Changchun 130022, China
 E-mail: ghuang@ciac.ac.cn
 xbzhang@ciac.ac.cn

[†] These authors contributed equally

of active materials and reducing the electrochemical polarization.^[17] In addition, the H-bond formed between molecules could increase their stability with reduced dissolution tendency in the electrolyte and accordingly realize improved cycle stability. Nevertheless, if the intensity of H-bond between the molecule and electrolyte exceeds a certain value, it will have negative effects, like facilitating the solubility of molecules in the electrolyte and thus shortening the battery lifetime. Therefore, the intensity of H-bond is a key factor in determining the stability and active site/material utilization at the same time. So, the biggest challenge is how to determine which kind of H-bond interaction is the optimal one? This requires us to design a series of H-bond based compounds with progressive relationships between the molecules, and molecule and the electrolyte to establish the correlation between the properties of H-bond and the battery performance.

Here, we have selected a family of quinone-based small molecules with progressive H-bond numbers to quantitatively disclose the effect of H-bond on the electrochemical performance of OEMs for ZIBs. It has been found that the introduction of H-bond could certainly improve the Zn^{2+} storage capability of OEMs, like capacity, voltage, lifetime, etc., and only the one with the equilibration of H-bond interaction between OEMs, and OEM and the electrolyte, here is 2,5-diaminocyclohexa-2,5-diene-1,4-dione (DABQ), realizes the full liberation of the performance. This means that the intensity of H-bond for the designed OEMs should be in an appropriate value, not too strong or too weak. With this in mind, the H-bond structure engineered DABQ delivers a reversible capacity of 376.3 mAhg^{-1} with an extremely low polarization of 20 mV, achieves 100% capacity retention after 1500 cycles at 5 Ag^{-1} , and even maintains a capacity of 194.3 mAhg^{-1} at a record-high mass loading of 66.2 mgcm^{-2} . These results verify that the utilization of the powerful H-bond weak interaction could conquer the long-lasting challenges of OEMs encountered in ZIBs, promoting the development of high-performance aqueous zinc-organic batteries.

Results and Discussion

Five quinone-based small molecules with a H-bond evolution model, including benzoquinone (BQ), 2,5-diaminocyclohexa-2,5-diene-1,4-dione (DABQ), 2,3,5,6-tetraaminocyclohexa-2,5-diene-1,4-dione (TABQ), 2,5-bis(methylamino)cyclohexa-2,5-diene-1,4-dione (MeDABQ), and 2,5-bis(dimethylamino)cyclohexa-2,5-diene-1,4-dione (DMeDABQ), were rationally selected and synthesized as cathode materials for ZIBs (Figure 1a), of which the theoretical specific capacities and the corresponding calculation details were listed in Figure S1. The structures of these quinones were confirmed by the nuclear magnetic resonance (NMR) spectroscopy and X-ray diffraction (XRD) patterns (Figure 1b and Figure S2). For the starting basic skeleton of BQ, although it has a high theoretical capacity (496 mAhg^{-1}), its independent para-carbonyl group cannot coordinate the divalent Zn^{2+} due to the weak

interaction between BQ molecules, and also BQ molecule and the electrolyte (Figure 1c), making BQ deliver an extremely low discharge capacity (Figure S3a). The weak interactions between the BQ molecules, and BQ molecule and the electrolyte have been demonstrated by the ab initio molecular dynamic calculations (AIMD) (Figure S4). Then, primary ammonia was introduced in the neighboring positions of the carbonyl groups of BQ to construct DABQ (step 1, Figure 1a). If introducing a single amino group, it will break the structural symmetry of BQ, making the chemical environment of the active sites become inconsistent and accordingly decrease the available capacity and structure stability. As can be seen from the Fourier transform infrared (FTIR) spectra in Figure S5a, the $-\text{NH}_2$ renders the $\text{C}=\text{O}$ stretching vibration redshift from 1772 cm^{-1} to 1662 cm^{-1} , indicating the formation of H-bond interaction.^[15] The existence of $-\text{NH}_2$ in DABQ could establish H-bond between both the structure skeleton and the DABQ and electrolyte, assisting the carbonyl group to capture of Zn^{2+} and also enhancing the thermodynamic stability of DABQ and its affinity to the electrolyte simultaneously (Figure S6–8). Moreover, different from the room-temperature sublimation of BQ under vacuum, the sublimation temperature of DABQ is much higher and can only start from 170°C (Figure S6), revealing that the formation of intermolecular H-bonds among DABQ could significantly increase its stability. This can be further demonstrated by the thermogravimetric analysis (TGA), where the DABQ shows a higher high-temperature resistance than BQ (Figure S7). Figure S8 gives the electrolyte contact angles (ECAs) test of the quinones. It is clear that the introduction of $-\text{NH}_2$ decreases the ECAs from 53.5 to 17.5° , implying that the creation of H-bond interaction between DABQ and electrolyte is beneficial for electrolyte to infiltrate into the electrode, thus reducing the interfacial resistance and improving the utilization rate of active materials. Considering the above beneficial effects brought by the H-bond interaction, the electrochemical performance of DABQ was checked. As indicated in Figure S3b, the DABQ could deliver a capacity of 376.3 mAhg^{-1} with clear discharge/charge platforms at an extremely low polarization, more than one orders larger than the capacity of BQ (12.5 mAhg^{-1}). The slightly irreversible charge capacity can be attributed to the competitive adsorption of OH^- and SO_4^{2-} on the amino radical cation at high charge potential, which results in undesired O_2 evolution reaction.^[18–20] The performance improvement of DABQ can be ascribed to the H-bond interaction between DABQs and DABQ and the electrolyte enabled increase of structural stability, utilization of active sites, and electrolyte wettability (Figure 1d). Then, a question would come, if further increase the H-bond number, will the performance continuous to improve? To answer this question, another two $-\text{NH}_2$ were introduced into DABQ to obtain TABQ (step 2, Figure 1a). Compared with DABQ, the TABQ has higher sublimation temperature and thermal stability, a smaller ECA, and the $\text{C}=\text{O}$ peak redshifts to 1666 cm^{-1} (Figure S5–8). To further clarify the effects of increasing the number of H-bond, in situ variable temperature FTIR of DABQ and TABQ was conducted

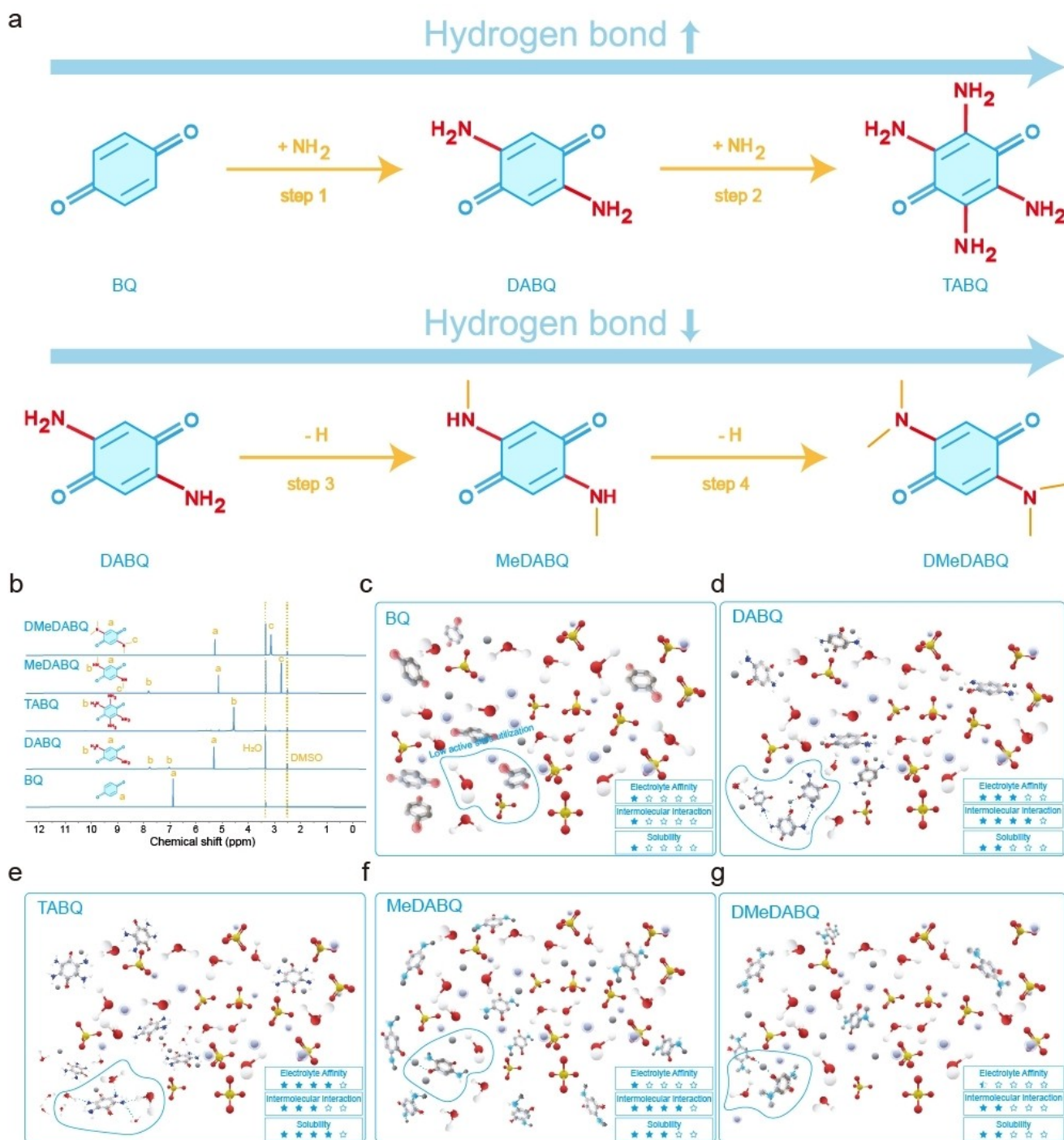


Figure 1. Design of H-bond evolution model for aqueous ZIBs. (a) Progressive and breakage model of the quinone-based H-bond structures. (b) ^1H NMR spectra of the above-mentioned five quinones. Schematic diagrams of the BQ (c), DABQ (d), TABQ (e), MeDABQ (f), and DMeDABQ (g) in aqueous ZIBs.

(Figure S9). As the rising of temperature, the symmetric and antisymmetric $-\text{NH}_2$ stretch bands for DABQ and TABQ blueshift, suggesting the high temperature could weak the H-bond interaction.^[21,22] Meanwhile, the redshift of carbonyl discloses that the H-bond could rarely form between the amino and carbonyl, and the intermolecular van der Waals interaction would dominate at high temperatures.^[23–25] Fur-

thermore, the high-temperature induced low-degree blueshift of $-\text{NH}_2$ and high-degree redshift of carbonyl uncovers that the increase of H-bond number could strengthen the intermolecular H-bond interaction. However, different from the situation under vacuum, when encountering the aqueous electrolyte, the increased number of $-\text{NH}_2$ makes the TABQ also form more H-bonds with the electrolyte and

accordingly weaken the intermolecular H-bond interaction (Figure 1e). This can be supported by the ^1H - ^1H NOESY analysis, which could provide information about the interactions between OEMs and OEM and the electrolyte. As shown in Figure S10a, the NOE cross peak between the $-\text{NH}_2$ and $-\text{NH}_2$ chemical shifts can be clearly observed for DABQ, meaning there are direct intermolecular H-bond interactions between DABQs.^[26] For TABQ, its four $-\text{NH}_2$ make it easier to form H-bond with water, reducing the intermolecular interactions and connections (Figure S10b). After getting the above information, the Zn^{2+} ion storage properties of TABQ were studied. Just as expected, it shows decreased capacity and increased voltage gap (Figure S3c). Meanwhile, the battery exhibits poor cycling stability due to the strong H-bond interaction between the TABQ and electrolyte (Figure S11), which renders accelerated dissolution of TABQ in the electrolyte. These results well respond to the above question: simply increasing the number of H-bonds does not always improve the performance, but will bring about opposite effect, that is, the H-bond should be in an appropriate value.

To further support the above conclusion, we selected another two derivatives (MeDABQ and DMeDABQ) of DABQ with reduced H-bond capabilities (Figure 1a, steps 3 and 4). As the H-bonds within the DABQ are continuously disrupted, the thermodynamic stability of the resulted MeDABQ and DMeDABQ gradually diminishes accompanied with an increase in the ECAs (Figure S6–8). This can be further confirmed by the blueshift observed in the $\text{C}=\text{O}$ band and the weak changes in the in situ variable temperature FTIR spectra (Figure S5b and Figure S12), which reveals that the decrease of H-bond number weakens the intermolecular H-bond interaction and also the interaction with the electrolyte (Figure 1f and 1g). Then, the electrochemical performance of MeDABQ and DMeDABQ was checked (Figure S13). For MeDABQ, although the substitution of the primary amino group's hydrogen with a hydrophobic methyl group has minimal impact on the reversible capacity, it leads to an increase in polarization (~ 70 mV) and a poor cycling lifetime (Figure S13a and S14). In addition, the existence of $-\text{Me}$ groups in MeDABQ could inhibit charge recombination and promote charge transfer, resulting in a stronger local charge redistribution and promoting the adsorption of oxygen intermediates. Also, the $-\text{Me}$ groups could induce the molecular configuration to produce *ortho* activation, making the *ortho* N adjacent to the $-\text{Me}$ group behave as the active centers to catalyze the dissolved oxygen in the electrolyte to occur ORR reaction and consequently contributing to additional discharge capacity.^[27,28] While for DMeDABQ with the complete substitution of the amino group's hydrogen with the methyl groups, it delivers limited capacity with a pretty poor reversibility (Figure S13b). Furthermore, the molecule structure of DMeDABQ would occur irreversible transformation due to the rotational freedom of methyl groups rendered formation of an unconjugated structure. This makes the reaction intermediates easily dissolve into the electrolyte during the discharge process and shuttle to the cathode-electrolyte interface to be continuously oxidized (even

oxidized to N radical cation ($\text{N}^{\bullet+}$) during the charge process, resulting in a large irreversible charge capacity.^[29] The above results suggest that the existence of H-bond is beneficial for the active sites of molecules to couple with the Zn^{2+} when the H-bond number falls within an appropriate range (Figure 1c–g). Also, it is clear that the DABQ with the most optimal H-bond interaction would be a potential high-performance cathode for ZIBs. In the following parts, its Zn^{2+} storage capability and mechanism were detailedly studied.

Coin-type organic//Zn batteries were assembled to evaluate the electrochemical performance of the synthesized quinone-based cathodes. The results show that the quinones (DABQ, MeDABQ) with appropriate H-bond interactions exhibit high utilization of active sites and small charge/discharge gaps when compared to those with weak/strong H-bond interactions (DMeDABQ, TABQ, Figure 2a). The presence of a suitable number of H-bond groups could make the H-bond interactions between quinones and the quinones and the electrolyte reach an optimal balance, resulting in increased utilization of both the active sites and active materials. However, an excessive number of H-bonds, like the saturation of H-bonds, would break this balance and accordingly significantly affect the performance liberation of the quinones with limited capacities. It should be noted that the average discharge potential of the quinones generally depends on their energy levels of the lowest unoccupied

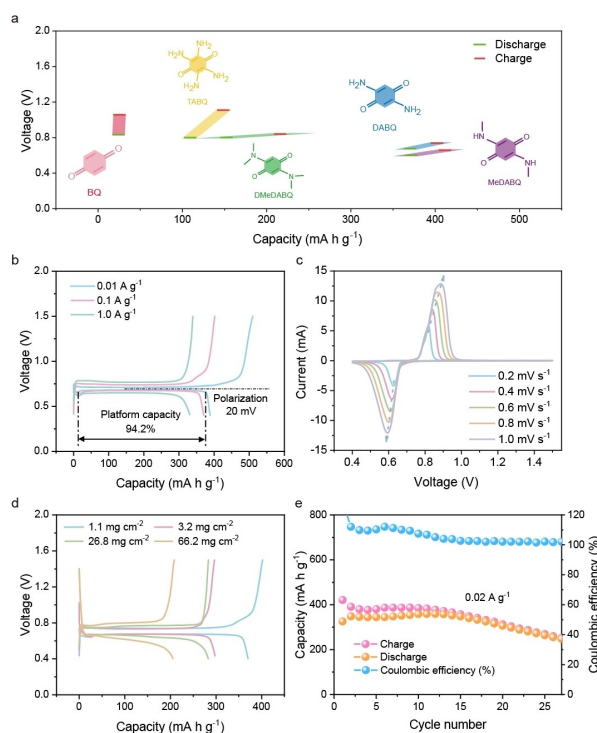


Figure 2. Electrochemical performance of the quinone-based cathodes in aqueous ZIBs. (a) Voltages and capacities of the five quinone-based cathodes. Discharge/charge (b) and CV (c) curves of DABQ//Zn batteries. (d) Discharge/charge curves of DABQ//Zn batteries with different loading masses at 0.1 A g^{-1} . (e) Cycle performance of the DABQ//Zn battery at 0.02 A g^{-1} .

molecular orbital (LUMO): a lower LUMO energy corresponds to a higher discharge potential (vide post).^[9,30] However, the introduction of four –Me groups significantly improve its catalytic activity for ORR, which has a higher onset-potential than the discharge voltage of DMeDABQ itself. As a result, the high voltage for inducing the ORR reaction makes the DMeDABQ exhibit a higher discharge voltage plat than the MeDABQ (Figure 2a). Among the five quinones, the DABQ with the most appropriate H-bond number could deliver a large capacity while maintaining a relatively high discharge voltage (Figure 2a).^[31] In particular, the DABQ exhibits a capacity of 376.3 mAh g⁻¹ with a utilization rate of carbonyls as high as 97% (Figure 2b). Even increased the current density from 0.01 to 0.1 and 1 A g⁻¹, the discharge capacities could still maintain 358.3 and 319.3 mAh g⁻¹, respectively, while the capacity contribution from the conductive CNTs is rather minimal (Figure S15). Moreover, the charge/discharge voltage polarization for DABQ is only 20 mV at 0.01 A g⁻¹ and 117 mV at 1 A g⁻¹ (Figure 2b), surpassing almost all the existing OEMs (Table S1). We have also calculated the ratio of the discharge platform capacity for the DABQ, which reaches 94.2%. This high value could guarantee a stable energy output, making it more suitable for large-scale energy storage systems without the need of complex voltage regulation devices.^[30]

Figure 2c depicts the typical cyclic voltammetry (CV) curves of the DABQ at various scan rates, providing information on the controlling factors of the storage/release of ions. A reduction peak corresponded to the conversion of C=O to C–O⁻ and an oxidation peak ascribed to the reversible reaction could be clearly observed. As indicated in Figure S16a, the peak current and the square root of the scan rate follow a linear relationship, suggesting that the diffusion process controls the ion uptake and removal behavior of DABQ.^[30] Additionally, the *b* values closer to 0.5 (*b_o*=0.50, *b_r*=0.65) further confirm the diffusion-controlled process of DABQ (Figure S16b). Despite this, the DABQ could achieve a high-capacity retention of over 76% at a loading mass of 26.8 mg cm⁻² (Figure 2d). Remarkably, even increased the loading mass by 60-fold (66.2 mg cm⁻², the diameter and thickness of this thick electrode are 10 mm and 0.84 mm, respectively), the DABQ could still deliver a large capacity of 194.3 mAh g⁻¹ (~11 mAh) with a well remained flat redox plateau (Figure 2d and S17), which has never been realized for OEMs at such a high loading mass (Table S1). This excellent loading capacity can be attributed to the appropriate interaction of DABQ monomers in the electrolyte environment. On the one hand, the suitable intermolecular interaction could effectively enhance the film-forming properties of the electrode, preventing the fragmentation of electrode under high loading mass of active materials; on the other hand, a good electrolyte affinity ability for DABQ would facilitate the ion arrival not only on the electrode surface but also in the bulk phase of active materials, which is particularly important for thick electrodes. Optimal interactions between DABQs, and DABQ and the electrolyte are simultaneously realized by its rational H-bond numbers (Figure S18),

enabling the successful preparation of high-mass-loading electrodes with improved electrochemical performance. Then, the rate performance of DABQ was studied. As increasing the current densities from 0.1 to 0.3, 0.5, 1, 3, and 5 A g⁻¹, decent capacities could be released and a capacity near 180.3 mAh g⁻¹ could be retained at 5 A g⁻¹ (Figure S19), demonstrating the rapid electrochemical response of the carbonyl in DABQ. Besides the high-rate capability, the DABQ also displays a satisfactory cycle stability with a capacity retention rate of >71% over 25 cycles at a small current density of 0.02 A g⁻¹ (Figure 2e), indicating that the appropriate H-bond interaction could well relieve the dissolution and structure damage issues of DABQ. Furthermore, the DABQ also exhibits excellent cycle stability with a 100% capacity retention (excluding the activation process) for over 1500 cycles at 5 A g⁻¹ (Figure S20). The superior ions storage capability of DABQ obtained here, like ultra-low charge/discharge potential gap, remarkable rate and cycling performance, demonstrates the effectiveness of the H-bond engineering on conquering the performance liberation limitations of small molecules, make DABQ a promising high-performance cathode for aqueous ZIBs.

After confirming the excellent electrochemical performance that DABQ could be delivered, density functional theory (DFT) calculations were employed to judge the specific active sites for Zn²⁺ ion uptake, verify the electron-donating/withdrawing effect, and infer the structural changes of DABQ following the Zn²⁺ uptake/remove. From the ESP mapping results we can see that the areas surrounding the carbonyls of the five quinones exhibit negative ESP values (Figure 3a–e), indicating their roles as active sites for Zn²⁺ storage/release during the discharge/charge process.^[32] Despite having the same active sites in terms of type, number, and position, these quinones exhibit significantly different electrochemical performances, which can be attributed to the influence of H-bond interaction between quinones and quinones and the electrolyte. Besides the H-bond effects, the incorporation of amino groups could also narrow the band gaps of quinones, providing further support for the rationality of the structural design (Figure 3f). Moreover, the values of the LUMO energy for the designed quinones, except for DMeDABQ, are consistent with the discharge potentials they displayed (Figure 2a).^[33] For DABQ, compared to the storage of one Zn²⁺ by a single molecule during the discharge process, the capture of Zn²⁺ by two adjacent molecules is found to be a more favorable reaction path, as it exhibits more negative Gibbs free energy changes (Figure 3g). After this, the optimized configuration of DABQ after Zn²⁺ uptake was calculated. As given in Figure 3h and 3i, an alternating structure of DABQ–Zn–DABQ with the majority of the molecules lying in a plane forms, which is in good agreement with the above favorable reaction path. The formation of this alternating structure is in closely related to the appropriate intermolecular H-bond interaction among DABQs. In addition, this structure arrangement also contributes to the reduced charge/discharge polarization of DABQ//Zn batteries.

Given the potential existence of multiple charge storage mechanisms in all OEMs encountered in aqueous ZIBs,

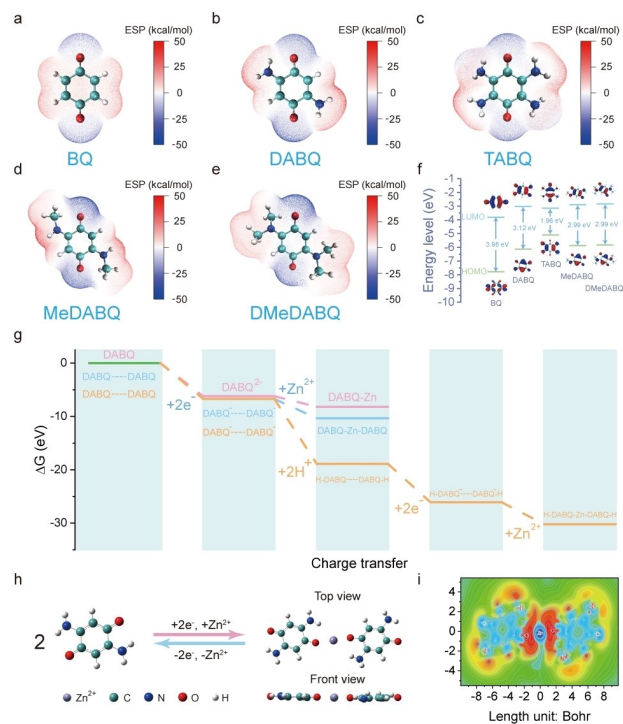


Figure 3. Theoretical calculations. The ESP mapped molecular van der Waals surface of BQ (a), DABQ (b), TABQ (c), MeDABQ (d), and DMeDABQ (e). (f) HOMO/LUMO energy levels and orbit distribution of the above five quinones. (g) The calculated Gibbs free energy gaps between DABQ and the related discharged states to clarify the reaction routes of the discharge process. Optimized configuration (h) and electron density gradient map (i) of DABQ after Zn ion uptake.

such as the individual storage of Zn^{2+} or H^+ , or co-storage of Zn^{2+} and H^+ , the non-aqueous electrolyte (involving only Zn^{2+}) was used to check the Zn^{2+} storage ability of DABQ. The reduction peak observed around 0.61 V and the 143.3 mAh g^{-1} discharge capacity delivered successfully confirm the Zn^{2+} involved electrochemical reactions for DABQ (Figure S21). To more clearly demonstrate the ion storage mechanism of DABQ, ^1H NMR spectra of the electrodes discharged in the H_2SO_4 and ZnSO_4 electrolytes have been presented in Figure S22a and b. Compared to the electrode in the H_2SO_4 electrolyte, the phenolic hydroxyl group exhibits clear decrease in proportion and signal shift to low magnetic fields for the electrode in the ZnSO_4 electrolyte, confirming the storage of Zn^{2+} in DABQ during the discharge process (Figure S22a). In addition, the H signal from the phenolic hydroxyl group emerges after discharging (Figure S22b) and subsequently disappears upon recharging the electrode in the ZnSO_4 electrolyte (Figure S22c), providing solid evidence for the H^+ involved storage process of DABQ. DFT calculations were then conducted to study the ion storage mechanism of DABQ from the thermodynamics point of view. As depicted in Figure 3g, the co-storage of Zn^{2+} and H^+ exhibits a relatively easier process compared to the storage of Zn^{2+} alone, indicating that the participation of H^+ can promote the storage of Zn^{2+} in the DABQ.^[34]

To further clarify the energy storage mechanism of DABQ, a series of ex situ characterizations were carried out to thoroughly investigate its structure and composition evolution during the charge and discharge processes. Figure 4a and 4b monitors the DABQ electrodes at various discharged and charged states using FTIR spectra. As the discharge process goes on, the peak corresponding to $\text{C}=\text{O}$ vibration at 1660 cm^{-1} experiences a continuous decrease in intensity (Figure 4b, from a to c). Simultaneously, the peak of $\text{C}-\text{O}^-$ at 1480 cm^{-1} gradually emerges, indicating the transformation of $\text{C}=\text{O}$ to $\text{C}-\text{O}^-$ anions accompanied with the uptake of H^+ and Zn^{2+} to balance the negative charges. Upon charging to 1.5 V, the peak intensity of $\text{C}=\text{O}$ and $\text{C}-\text{O}^-$ exhibits a reverse trend, manifesting the reversible transformation from $\text{C}-\text{O}^-$ back to $\text{C}=\text{O}$ (Figure 4b, from d to f).^[35] Furthermore, the appearance of a characteristic peak from the stretching vibration of $-\text{OH}$ at around 3350 cm^{-1} during the discharge process and its existence in the subsequent recharge process reveals the stored cations containing H^+ in DABQ (Figure S23). It is worth noting that the discharged electrodes could be oxidized by air due to its air rechargeability (vide post), leading to the transformation from $\text{C}-\text{O}^-$ back to $\text{C}=\text{O}$ during the test process of the ex situ FTIR measurement. To accurately explore the evolution process of $\text{C}=\text{O}$, in situ FTIR and Raman spectroscopy during the charge/discharge process were supplemented. Figure S24a and b clearly shows the reversible change of $\text{C}=\text{O}$ during cycling, certifying the high reversibility of active sites. Then, XPS spectra of the DABQ electrodes at different stages were acquired to further elucidate its ion storage mechanism (Figure 4c), which clearly certifies the storage and release of Zn^{2+} in the DABQ during the discharge and charge processes. Addi-

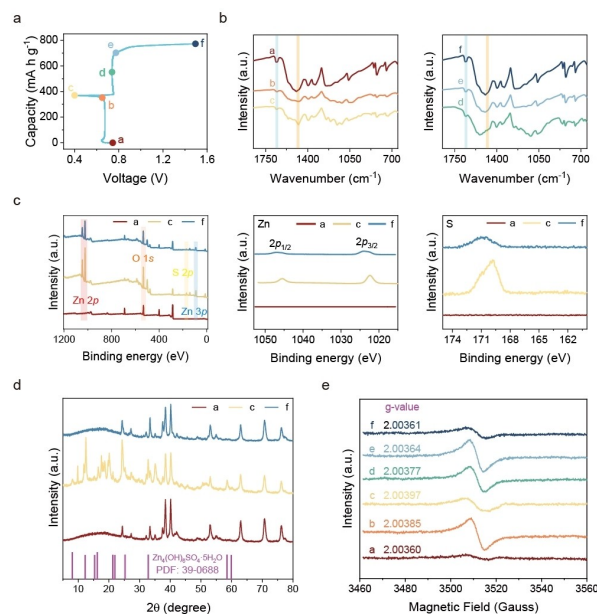


Figure 4. Energy storage mechanism of DABQ. Discharge/charge curves (a) and corresponding FTIR (b), XPS (c), XRD (d), and EPR (e) spectra of DABQ at various electrochemical states.

tionally, the atomic ratio of Zn and S for the fully discharged electrode in the ZnSO_4 electrolyte is 20.6 (Figure S25), much larger than the 4 for $\text{Zn}_4(\text{OH})_6\text{SO}_4 \cdot 5\text{H}_2\text{O}$, indicating the XPS signal of Zn originates from both the DABQ stored Zn^{2+} and $\text{Zn}_4(\text{OH})_6\text{SO}_4 \cdot 5\text{H}_2\text{O}$. This conclusion can be further supported by the inductively coupled plasma (ICP) result, in which the Zn:S mole ratio of the discharged electrode in the ZnSO_4 electrolyte is ~ 18.4 . To verify the existence of $\text{Zn}_4(\text{OH})_6\text{SO}_4 \cdot 5\text{H}_2\text{O}$, scanning electron microscope (SEM) images of the DABQ electrodes at different electrochemical states were checked (Figure S26). As the discharge process goes on, the appearance of micro/nano flakes agrees well with the typical morphology of $\text{Zn}_4(\text{OH})_6\text{SO}_4 \cdot 5\text{H}_2\text{O}$. Upon charging to 1.5 V, there is still some residual $\text{Zn}_4(\text{OH})_6\text{SO}_4 \cdot 5\text{H}_2\text{O}$, indicating the incomplete decomposition of $\text{Zn}_4(\text{OH})_6\text{SO}_4 \cdot 5\text{H}_2\text{O}$ and consistent with the XRD result (Figure 4c). In the ZnSO_4 electrolyte, OH^- would continuously generate through the consumption of H^+ in DABQ during the discharge process. The formed OH^- can react with ZnSO_4 to form $\text{Zn}_4(\text{OH})_6\text{SO}_4 \cdot 5\text{H}_2\text{O}$ (Figure 4c and S27).^[36] The emergence of the S 2p peak can be ascribed to the H^+ consumption induced formation of $\text{Zn}_4(\text{OH})_6\text{SO}_4 \cdot 5\text{H}_2\text{O}$ (Figure 4d). Since the occurrence of Zn^{2+} and H^+ co-storage behavior in DABQ, DABQ–Zn and $\text{Zn}_4(\text{OH})_6\text{SO}_4 \cdot 5\text{H}_2\text{O}$ would simultaneously generate (atomic ratio of Zn:S=20.6) during the discharge process. For the charged electrode, the atomic ratio of Zn and S is close to 4 (Figure S25), same as the $\text{Zn}_4(\text{OH})_6\text{SO}_4 \cdot 5\text{H}_2\text{O}$, indicating the remnant of undecomposed $\text{Zn}_4(\text{OH})_6\text{SO}_4 \cdot 5\text{H}_2\text{O}$ and high reversibility of DABQ towards Zn ion storage. The presence or absence of DABQ–Zn leads to the chemical environment change of $\text{Zn}_4(\text{OH})_6\text{SO}_4 \cdot 5\text{H}_2\text{O}$, thus resulting in the peak shift of Zn 2p and S (Figure 4c). In addition, the O 1s XPS spectra also provide powerful evidence for the reversible transformation between C=O and C–O⁻ during a single cycle process (Figure S28). Aside from the FTIR and XPS measurements, ex situ electron paramagnetic resonance (EPR) spectra were also recorded to validate the ion storage mechanism of DABQ. Figure 4e shows the almost reversible shift of the g value during the discharge/charge process. For the intermediate states (b, e, and d), the peak intensity increases due to the higher concentration of the radical species (C–O⁻) and decreases at the fully charged/discharged states (c and f). The relatively narrow peak shape at the intermediate states can be attributed to the localization of the unpaired electron at the O atoms after undergoing one electron reduction of DABQ with the uptake of H^+ . This process could increase the electron cloud density around the oxygen and thus ensuring a high utilization of the active sites. The wider peak shape observed at the fully charged/discharged states is due to the electron delocalization, which ensures the stability of the DABQ structure during the long-term cycling process.^[29] Notably, both the g value and the peak shape of the DABQ do not fully recover to the pristine state (a) after charging (f), attributing to the generation of a small amount of amino radical cation. To sum up, the above results strongly support the occurrence of Zn^{2+} , H^+ (de)storage behavior in DABQ during the discharge/charge

process, which is in good accordance with the calculation results.

The Zn^{2+} , H^+ (de)coordination behavior and the unique coordination configuration of the discharged state (H–DABQ–Zn–DABQ–H) result in an inhomogeneous distribution of charge in the DABQ monomers, weakening the electron density of the outside C=O part. This decreased electronegativity could reduce the extraction energy of H^+ , making the air-induced spontaneous oxidation of the discharged DABQ become possible.^[37,38] Consequently, a self-powered battery system as a proof-of-concept demonstration was constructed to realize the green battery goal that is charged by the ubiquitous and cost-free air. During the air-charging process, the potential continuously rises due to the large potential gap between the oxygen and discharged DABQ accompanied by the extraction of H^+ (Figure 5a), resulting in the recovery of the battery energy without the need for an external power supply. Moreover, the voltage and discharge capacity increase as the air-charging time prolongs, and the discharge platform remains consistent with the power charge/discharge mode. To elucidate the air-charging mechanism, ex/in situ FTIR analysis was conducted on the DABQ cathodes at different stages. As shown in Figure S29, the peak intensity of C=O vibration enhances with the extension of the air-charging duration, indicating the gradual oxidation of C–O⁻ to C=O with the help of the air. This process can be further confirmed by the in situ FTIR analysis in Figure 5b. During the air-charging process, the intensity of the carbonyl vibration peak strengthens, while the signal of the –OH moiety gradually weakens, corresponding to the air-rendered extraction of H^+ with the transformation of C–O⁻ to C=O.

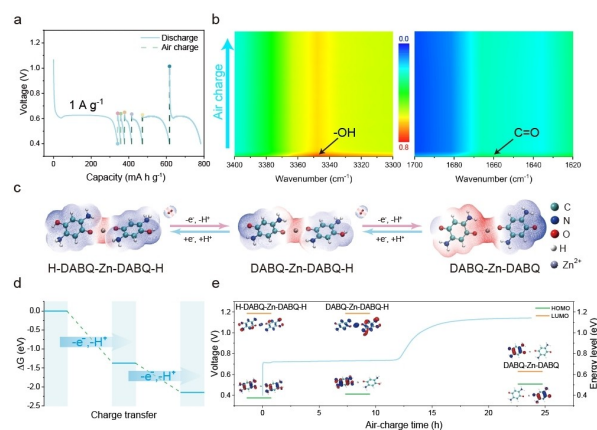


Figure 5. Air-charging performance of DABQ//Zn batteries. (a) The galvanostatic discharge curves at 1 A g^{-1} after different air-charging times. (b) In situ FTIR spectra during the air-charging process. (c) Structural evolution and MESP distribution on the van der Waals surface of the H–DABQ–Zn–DABQ–H molecule and the related charge products during air-charging process. (d) The calculated Gibbs free energy gaps between H–DABQ–Zn–DABQ–H molecule and the related air-charging states. (e) HOMO/LUMO energy levels and orbit distribution of H–DABQ–Zn–DABQ–H molecule and corresponding charge products.

To further clarify the structure evolution of the discharged DABQ during the air-charging process, theoretical calculations were conducted to simulate the process of H^+ extraction. Figure 5c gives the molecular electrostatic potential (MESP) of H–DABQ–Zn–DABQ–H and its associated charge products. As H^+ extraction involves a nucleophilic reaction, the most probable extraction sites are located around the positive regions on MESP. Therefore, the –OH moieties of H–DABQ–Zn–DABQ–H are determined to be the H^+ extraction sites, aligning with the in situ FTIR result (Figure 5b).^[37] After getting this information, the Gibbs free energy change of H–DABQ–Zn–DABQ–H during the H^+ extraction process was analyzed (Figure 5d). It is clear that the air-induced recharge of the discharged DABQ is a spontaneous reaction with a negative value of ΔG . Additionally, the energy levels of H–DABQ–Zn–DABQ–H, DABQ–Zn–DABQ–H, and DABQ–Zn–DABQ were also calculated (Figure 5e). The observed increase in LUMO energy from H–DABQ–Zn–DABQ–H to DABQ–Zn–DABQ correlates well with the increase in voltage, again confirming the air-induced recharge process (Figure 5e). To check the practical application ability, a large-sized DABQ//Zn battery was assembled to illumine a LED panel (Figure S30). Following the depletion of the battery power, the DABQ cathode was exposed to the air to initiate the air-charging process. As expected, the re-powered DABQ//Zn battery possesses enough energy to re-light the LED panel, demonstrating the practicality of the developed air-rechargeable ZIBs. This self-powered ability of the DABQ//Zn battery does not depend on the geographical environmental conditions, which is of vital importance for the activities without external power supply.

Conclusion

In summary, a series of quinone-based small molecules with progressive H-bond numbers has been rationally selected to shed light on the real effects of H-bond on the electrochemical performance of OEMs for ZIBs. It has been found that only the appropriate number of H-bond could make the interaction between OEMs and OEM and the electrolyte realize an optimal balance, contributing to stabilizing the molecular structure during cycling, enhancing the utilization of active sites and active materials, and reducing the battery polarization. As a result, the DABQ featuring with the most appropriate H-bond number exhibits a high capacity of 376.3 mAhg^{-1} (97% utilization of the active sites) and a record-low charge–discharge potential gap of 20 mV at 10 mA g^{-1} , and also a 100% capacity retention after 1500 cycles at 5 Ag^{-1} . Even increased the loading mass to 66.2 mg cm^{-2} , the DABQ could still deliver a reversible capacity above 193.3 mAhg^{-1} , which has never been achieved before. Besides the excellent electrochemical performance, the DABQ//Zn battery also possesses an air-recharging ability with the possibility of long-term operation in the areas without external power supply. This study presents that the rational design of OEMs with an appropriate H-bond number is a powerful strategy to addressing

the thorns that restrict the construction of high-performance ZIBs.

Acknowledgements

This work was financially supported by the National Key R&D program of China (Grant 2022YFB2402200), National Natural Science Foundation of China (Grant 52271140, 52171194), Jilin Province Science and Technology Development Plan Funding Project (Grant YDZJ202301ZYTS545), National Natural Science Foundation of China Excellent Young Scientists (Overseas), and Youth Innovation Promotion Association CAS (Grant 2020230).

Conflict of Interest

The authors declare no conflict of interest.

Data Availability Statement

The data that support the findings of this study are available from the corresponding author upon reasonable request.

Keywords: Hydrogen Bond · Organic Electrode Materials · Aqueous Zinc-Organic Batteries · Quinone · Air-Rechargeable

- [1] J. Li, N. Sharma, Z. Jiang, Y. Yang, F. Monaco, Z. Xu, D. Hou, D. Ratner, P. Pianetta, P. Cloetens, F. Lin, K. Zhao, Y. Liu, *Science* **2022**, *376*, 517–521.
- [2] H. Xia, Y. Tang, O. I. Malyi, Z. Zhu, Y. Zhang, W. Zhang, X. Ge, Y. Zeng, X. Chen, *Adv. Mater.* **2021**, *33*, 2004998.
- [3] M. Fan, X. Chang, Q. Meng, L. J. Wan, Y. G. Guo, *SusMat* **2021**, *1*, 241–254.
- [4] F. Wan, L. Zhang, X. Wang, S. Bi, Z. Niu, J. Chen, *Adv. Funct. Mater.* **2018**, *28*, 1804975.
- [5] H. Zhang, Y. Fang, F. Yang, X. Liu, X. Lu, *Energy Environ. Sci.* **2020**, *13*, 2515–2523.
- [6] T. P. Nguyen, A. D. Easley, N. Kang, S. Khan, S. M. Lim, Y. H. Rezenom, S. Wang, D. K. Tran, J. Fan, R. A. Letteri, X. He, L. Su, C. H. Yu, J. L. Lutkenhaus, K. L. Wooley, *Nature* **2021**, *593*, 61–66.
- [7] J. Wang, A. E. Lakraychi, X. Liu, L. Siew, C. Morari, P. Poizot, A. Vlad, *Nat. Mater.* **2021**, *20*, 665–673.
- [8] Z. P. Song, H. S. Zhou, *Energy Environ. Sci.* **2013**, *6*, 2280–2301.
- [9] Y. Lu, Q. Zhang, L. Li, Z. Q. Niu, J. Chen, *Chem* **2018**, *4*, 2786–2813.
- [10] Y. Lu, X. Hou, L. Miao, L. Li, R. Shi, L. Liu, J. Chen, *Angew. Chem. Int. Ed.* **2019**, *58*, 7020–7024.
- [11] S. Li, J. D. Lin, Y. M. Zhang, S. L. Zhang, T. Jiang, Z. L. Hu, J. J. Liu, D. Y. Wu, L. Zhang, Z. Q. Tian, *Adv. Energy Mater.* **2022**, *12*, 2201347.
- [12] Y. Lu, J. Chen, *Nat. Chem. Rev.* **2020**, *4*, 127–142.
- [13] L. Wang, J. Yan, Y. Hong, Z. Yu, J. Chen, J. Zheng, *Sci. Adv.* **2023**, *9*, eadf4589.
- [14] Z. Lin, H. Y. Shi, L. Lin, X. Yang, W. Wu, X. Sun, *Nat. Commun.* **2021**, *12*, 4424.
- [15] S. Zheng, D. Shi, T. Sun, L. Zhang, W. Zhang, Y. Li, Z. Guo, Z. Tao, J. Chen, *Angew. Chem. Int. Ed.* **2023**, *62*, e202217710.

- [16] Y. R. Wang, M. Liu, G. K. Gao, Y. L. Yang, R. X. Yang, H. M. Ding, Y. Chen, S. L. Li, Y. Q. Lan, *Angew. Chem. Int. Ed.* **2021**, *60*, 21952–21958.
- [17] X. T. Zhang, J. X. Li, H. S. Ao, D. Y. Liu, L. Shi, C. M. Wang, Y. C. Zhu, Y. T. Qian, *Energy Storage Mater.* **2020**, *30*, 337–345.
- [18] N. Wang, Z. Guo, Z. Ni, J. Xu, X. Qiu, J. Ma, P. Wei, Y. Wang, *Angew. Chem. Int. Ed.* **2021**, *60*, 20826–20832.
- [19] X. Dong, H. Yu, Y. Ma, J. L. Bao, D. G. Truhlar, Y. Wang, Y. Xia, *Chem. Eur. J.* **2017**, *23*, 2560–2565.
- [20] J. Luo, W. T. Wei, *Adv. Synth. Catal.* **2018**, *360*, 2076–2086.
- [21] H. Yan, M. Zhao, X. Feng, S. Zhao, X. Zhou, S. Li, M. Zha, F. Meng, X. Chen, Y. Liu, D. Chen, N. Yan, C. Yang, *Angew. Chem. Int. Ed.* **2022**, *61*, e202116059.
- [22] G. D. Wu, Y. N. Liu, Y. F. He, J. T. Feng, D. Q. Li, *Appl. Catal. B* **2021**, *291*, 120061.
- [23] J. Yi, C. Y. Liu, Y. Y. Tian, K. Wang, X. Y. Liu, L. B. Luo, *Polymer* **2021**, *218*, 123488.
- [24] J. H. Hu, R. K. Li, C. Chen, Z. Lu, K. Zeng, G. Yang, *Polymer* **2018**, *146*, 133–141.
- [25] L. Jiao, Z. J. Du, X. M. Dai, H. F. Wang, Z. X. Dong, H. B. Yao, X. P. Qiu, *Eur. Polym. J.* **2022**, *173*, 111260.
- [26] M. R. Tuttle, S. T. Davis, S. Zhang, *ACS Energy Lett.* **2021**, *6*, 643–649.
- [27] Z. You, B. Wang, Z. Zhao, Q. Zhang, W. Song, C. Zhang, X. Long, Y. Xia, *Adv. Mater.* **2022**, *35*, 2209129.
- [28] L. Su, L. Liu, B. Liu, J. Meng, X. Yan, *iScience* **2020**, *23*, 100995.
- [29] Z. Tian, V. S. Kale, Y. Wang, S. Kandambeth, J. Czaban-Jozwiak, O. Shekhah, M. Eddaoudi, H. N. Alshareef, *J. Am. Chem. Soc.* **2021**, *143*, 19178–19186.
- [30] Q. Zhao, W. Huang, Z. Luo, L. Liu, Y. Lu, Y. Li, L. Li, J. Hu, H. Ma, J. Chen, *Sci. Adv.* **2018**, *4*, eaao1761.
- [31] X. Yang, Y. Ni, Y. Lu, Q. Zhang, J. Hou, G. Yang, X. Liu, W. Xie, Z. Yan, Q. Zhao, J. Chen, *Angew. Chem. Int. Ed.* **2022**, *61*, e202209642.
- [32] Z. Chen, H. L. Cui, Y. Hou, X. Q. Wang, X. Jin, A. Chen, Q. Yang, D. H. Wang, Z. D. Huang, C. Y. Zhi, *Chem* **2022**, *8*, 2204–2216.
- [33] Z. Song, L. Miao, H. Duan, L. Ruhlmann, Y. Lv, D. Zhu, L. Li, L. Gan, M. Liu, *Angew. Chem. Int. Ed.* **2022**, *61*, e202208821.
- [34] S. Li, C. Huang, L. Gao, Q. Shen, P. Li, X. Qu, L. Jiao, Y. Liu, *Angew. Chem. Int. Ed.* **2022**, *61*, e202211478.
- [35] Y. J. Gao, G. F. Li, F. Wang, J. Chu, P. Yu, B. S. Wang, H. Zhan, Z. P. Song, *Energy Storage Mater.* **2021**, *40*, 31–40.
- [36] Y. Chen, J. Li, Q. Zhu, K. Fan, Y. Cao, G. Zhang, C. Zhang, Y. Gao, J. Zou, T. Zhai, C. Wang, *Angew. Chem. Int. Ed.* **2022**, *61*, e202116289.
- [37] Z. Tie, Y. Zhang, J. Zhu, S. Bi, Z. Niu, *J. Am. Chem. Soc.* **2022**, *144*, 10301–10308.
- [38] F. Yue, Z. Tie, Y. Zhang, S. Bi, Y. Wang, Z. Niu, *Angew. Chem. Int. Ed.* **2022**, *61*, e202208513.

Manuscript received: April 5, 2024

Accepted manuscript online: May 5, 2024

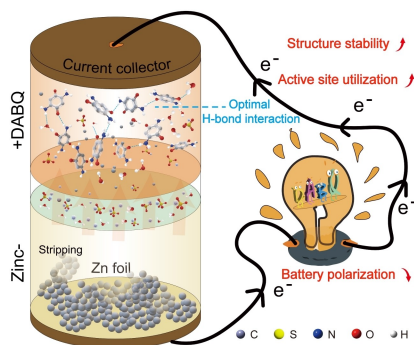
Version of record online: ■■■, ■■■

Research Articles

Aqueous Organic Batteries

J. Guo, J.-Y. Du, W.-Q. Liu,* G. Huang,* X.-B. Zhang* [e202406465](#)

Revealing Hydrogen Bond Effect in Rechargeable Aqueous Zinc-Organic Batteries



A series of quinone-based small molecules with progressive hydrogen bond (H-bond) numbers has been rationally designed to reveal the real effects of H-bond on the electrochemical performance of organic electrode materials (OEMs) in rechargeable aqueous zinc-organic batteries (ZOBs). The appropriate number of H-bonds in OEM improves its structure stability and utilization of active sites and reduces the battery polarization, contributing to the construction of high-performance ZOBs.